Supporting Information

Carbon Nitride Phosphorus as an Effective Lithium Polysulfide Adsorbent for

Lithium–Sulfur Batteries

Vandung Do[a,b,+], Deepika[c,+], Mun Sek Kim[a], Min Seop Kim[a,d], Kwang Ryeol Lee[c,], Won Il Cho[a,*]*

[a.]*Center for Energy Storage Research, Korea Institute of Science and Technology, Seoul, 02792, Republic of Korea.*

[b.]*Division of Energy and Environmental Technology, Korea University of Science and Technology (UST), Daejeon 34113 (Republic of Korea).*

[c.]*Computational Science Research Center, Korea Institute of Science and Technology, Seoul, 02792, Republic of Korea.*

[d.]*Department of Materials Science and Engineering, Korea University, Seoul, 02841, Republic of Korea.*

+: V.D. Do and Deepika contributed equally to this work.

*Email: wonic@kist.re.kr (W. I. Cho)

*Email: krlee@kist.re.kr (K. R. Lee)

Electrochemical performance test

The electrolyte was prepared by dissolving 1M LiTFSI in 1:1 (v/v) DOL and 1,2-dimethoxyethane (DME) (all from Sigma-Aldrich, 99.8%) containing 0.25 M $LiNO_3$ (JUNSEI, 99.5%). The coin cells CR 2032 were assembled in a standard dry room with the pristine PF, CNP0/PF, and CNP22/PF inserted between the S cathode and Li metal. Galvanostatic tests were conducted in a voltage window of 1.7–2.8 V at 25 °C using MACCOR 4000 battery-testing instrument. Cyclic voltammetry (CV) measurements of the Li–S cells were performed by the station BIOLOGIC instrument at sweep rate of 0.05 mV s^{-1}, within the voltage window of 1.7–2.8 V. Li–S cells with high S loading of 6.1 mg cm^{-2} on the cathode and CNP22/PF were tested in both voltage windows of 1.7–2.45 V and 1.7–2.8 V. The electrochemical impedance spectroscopy (EIS) tests on coin cells were carried out in the frequency range from 500 KHz to 0.1 Hz with a perturbation amplitude of 5 mV.

Material characterization

Powder X-ray diffraction (XRD) (Rigaku P/max 2200VPC) using Cu-Kα (λ=0.15406 nm) radiation was employed to verify the crystalline phase. The S percentage in the composite and the cathode was determined by TGA (SDT-Q600 TA Instruments) from RT to 550 °C in N_2 flow at a heating rate of 5 °C min^{-1}. The thermal stability of the CNPx was also evaluated by TGA from RT to 850 °C in N_2 flow at a heating rate of 5 °C min^{-1} (Figure S12). The XPS investigation was performed with a monochromator Al-Kα (1486.6 eV) anode (24.5 W, 15 kV) (Ultra-PHI). The high-resolution element mapping of CNP materials was performed using scanning transmission electron microscopy (STEM) with an FEI Tecnai G2-F30 TEM/STEM field-emission microscope equipped with a large solid angle for high X-ray throughput and a Gatan imaging filter for energy-filtered imaging. The BET and BJH measurements were performed using an ASAP 2020 Plus

Physisorption instrument. The elemental percentages of the CNPx were characterized by SEM-EDX using an Inspect F50–FEI system. The thickness of the CNP/carbon layer and its corresponding surface images were measured by the Step function with a 3D laser microscope (OLS4100). The absorption spectra of the Li_2S_6 in electrolyte solutions were acquired by the UV-Vis spectrophotometer UV-2550, SHIMADZU. For the color change test of the electrolyte solutions containing LiPS, 50 mg of CNP0 and CNP22 were added into two vials followed by the addition of 3 ml of LiTFSI electrolyte per vial. A vial containing only the electrolyte was used as a reference sample. Then, 0.2 ml of a 1M Li_2S_6 solution was added to each vial, and the color change was recorded by taking photographs.

High-S-loaded cathode fabrication

An aqueous binder system containing polyvinylpyrrolidone, carboxy-methyl cellulose and poly(ethylene oxide) in a weight ratio of 5:1:4 was dissolved in DI water (noted as PCP binder) and used for preparing all of the S composite slurries in this work. All of such polymers were purchased from Sigma-Aldrich and used directly without any treatment. The sulfur/carbon (S/C) composite was synthesized by first mixing the commercial carbon Ketjen Black 600JD (LION) and S powder (Aldrich, 99.998%) in a weight ratio of 4:1. The mixture of S/C was treated by melting diffusion in a vacuum oven at 155 °C for 10 hours. The composite was washed with DI water and ethanol and dried in an 80 °C oven for 24 hours. The S cathode was fabricated by ball milling the S/C composite, super P and PCP binder (ratio of 82/10/8 wt%), and then the slurry was uniformly spread onto the Al foil and dried at 60 °C for 24 hours in a vacuum oven. The percentage of pure S in the S/C composite (80%) and in the cathode (66%) was confirmed by TGA as seen in Figure S12. The S loading and the total S amount on the cathode (14 mm diameter) were *ca.* 3.2

mg cm^{-2} and 4.92 mg, respectively. For high-S-loaded cathodes, electrodes with 6.1 and 8.2 mg cm^{-2} of pure S were also fabricated.

Computational details

First principle calculations were performed using DFT as implemented in the Vienna *ab initio* simulations package (VASP)[1] to understand the adsorption behavior of LiPS molecules on the CNP monolayer. The generalized gradient approximation proposed by Perdew, Burke, and Ernzerhof (PBE) was employed to understand the electron-correlation interaction.[1] For the estimation of electron-ion interactions, the projected augmented wave formalism (PAW) formalism was used. All the atoms were relaxed until the force on each atom was ≤ 0.001 eV A^{-1}.[2] Convergence tests were performed for the optimum value of the lattice constant, k-points and cut-off energy before computing the final ground-state energies and other electronic properties. An energy cut-off of 550 eV was used to restrict the plane wave basis set. A vacuum layer of 15 Å was used to avoid the interlayer interactions.[3] The K-space sampling of the 1st Brillouin zone was performed using a Monkhorst-k space mesh[4] of 25x25x1 for CNP optimization, while 3x3x1 was used for the adsorption of LiPS on the surface of the substrate. A denser mesh of 5x5x1 was used to estimate the density of states for the adsorption of LiPS on CNP. A single K-point was considered to optimize the LiPS molecules under a cubic unit cell of 20 Å. The band structure of CNP was calculated using a Hybrid GGA, HSE06 functional. van-der Waals interactions were incorporated to consider the long-range interactions between the LiPS and the substrate using the vDFT-DF functional. The formation energy (E_f) at various concentrations of P in CNP was calculated using:

$$E_f = E_{CNP22} - E_{CNP0} + n_c\mu_c - n_p\mu_p \qquad (1)$$

Here, E_{CNP22} and E_{CNP0} are the free energies of CNP22 and CNP0, respectively; n_c and n_p are the numbers of C and P atoms substituted respectively; and μ_c and μ_p are the chemical potentials for C and P, respectively. The binding energy (BE) of the LiPS (ΔE) molecules on the various substrates was calculated using:

$$\Delta E = E(total) - [E(substrate) + E(LiPS)] \quad (2)$$

Here, *E(LiPS)* and *E(substrate)* are the free energies of the LiPS molecules and substrate before the adsorption of molecules; *E(total)* is the substrate energy after the adsorption of LiPS. A negative value of the BE emphasizes the bound state having attractive interactions between LiPS and the substrate. Charge density difference calculations were also performed for the qualitative analysis of the interactions between LiPS and CNP22,

$$\Delta\rho = \rho(total) - [\rho(LiPS) + \rho(CNP22)] \quad (3)$$

$\Delta\rho$, $\rho(total)$, $\rho(LiPS)$, and $\rho(CNP22)$ are the charge density difference, the density of CNP after LiPS adsorption, the density of LiPS, and the density of CNP before adsorption, respectively. Further, a Bader charge analysis was also performed to estimate the charge transfer between the adsorbed LiPS and the substrate.

Optimization of P concentration in CNP

The CNP properties varied with changes in the P concentrations, therefore, further experiments were performed to optimize the concentration of P in CNP. The respective formation energies were calculated for P concentrations ranging from 7.2% to 36% by atomic weight. The differences among the P concentrations in CNP were determined by energy-dispersive X-ray spectroscopy (EDX) with scanning electron microscopy (SEM); the results are shown in Figure S13. The thermal stabilities of all the CNPx samples were determined by TGA from room temperature to

850 °C (Figure S5). Note that TGA was used to determine the degree of structural stability of a material. The TGA results in Figure S5 show that CNP0 decomposes totally at 683 °C, whereas CNP22 retains 70% of its initial weight and stabilizes at 43% at 850 °C. Notably, the CNP22 formation is an exothermic process (Figure S14a), which corresponds to the thermodynamic release of energy, and thus provides the most stable CNP configuration.[5] This inverted energetic process of CNP22 directs the substitution of all the C_1 atoms (edge C of the heptazine ring, as shown in the inset of Figure S14a) to create a more symmetric and stable structure than those of its counterpart CNP configurations. A higher yield of CNP can therefore be obtained and can replace CNP0 in Li–S batteries. The electrochemical properties of CNP were then investigated to determine its suitability for use in Li–S systems. The electrochemical behavior of CNP was examined by the cyclic voltammetry (CV) investigation of CNP-containing Li–S cells (see the experimental section). The cyclic voltammograms at 0.05 mV s^{-1} (Figure S14b) show a shift in the anodic peak of the CNP samples with various P contents. However, there is no shift of the cathodic peak. There are also significant differences among the current responses of the CNP samples during cathodic sweeps at 2.03 and 2.32 V. This result is attributed to the discharge of the Li–S cells.[6] The cathodic peak intensity, especially at 2.03 V, increases from that for the cell with CNP7.2, reaches a maximum value of ~4.2 mA for the Li|CNP22/PF|S cell, and then decreases for higher P concentrations (CNP29 and CNP36). Although the interfacial impedance values of the cells with CNP with different P contents do not change significantly, Nyquist plots show fast electrode kinetics for the Li|CNP22/PF|S cell (Figure S14c). The smallest semicircle diameter in the impedance curve is observed for the Li|CNP22/PF|S cell, which indicates that the interfacial impedances in the cell are the lowest. The CV and EIS results show that the Li|CNP22/PF|S cell possesses the optimum properties; this is in agreement with the theoretical results. The cycling

performances of the Li–S cells with various CNPx/PF samples are shown in Figure S14d. The Li|CNP22/PF|S cell gives the best performance and retains a discharge capacity of 890 mAh g^{-1} after 50 cycles, which is 3.8% and 7.7% higher than that of CNP14 and CNP7.2, respectively. The detailed analysis in Figure 2 shows that in addition to the better electrical conductivity, the replacement of three C atoms by P atoms to generate CNP22 increases the number of the covalent bonds between the P and S atoms, increasing the LiPS adsorption capacity to the highest level, minimizing shuttling and maintaining the high electrochemical performance of the Li-S cells. The percentage of P atoms in CNP22 is large enough to produce LiPS adsorption interactions, however, we hypothesis that increasing the percentage of P atoms by 29 and 36% would not be effective for the electrochemical performance (Figure S14b-d) due to the increase in the level of impurities (here, it is O) in CNP (as seen in Figure S13e, f) that might negatively affect the LiPS adsorption capability of CNP. This high concentration of O might impede LiPS adsorption capability on CNP. Therefore, CNP22 has better performance than the others due to stronger interactions between LiPS and CNP22, which means that CNP22 has the optimum P concentration for PF modification in Li–S systems.
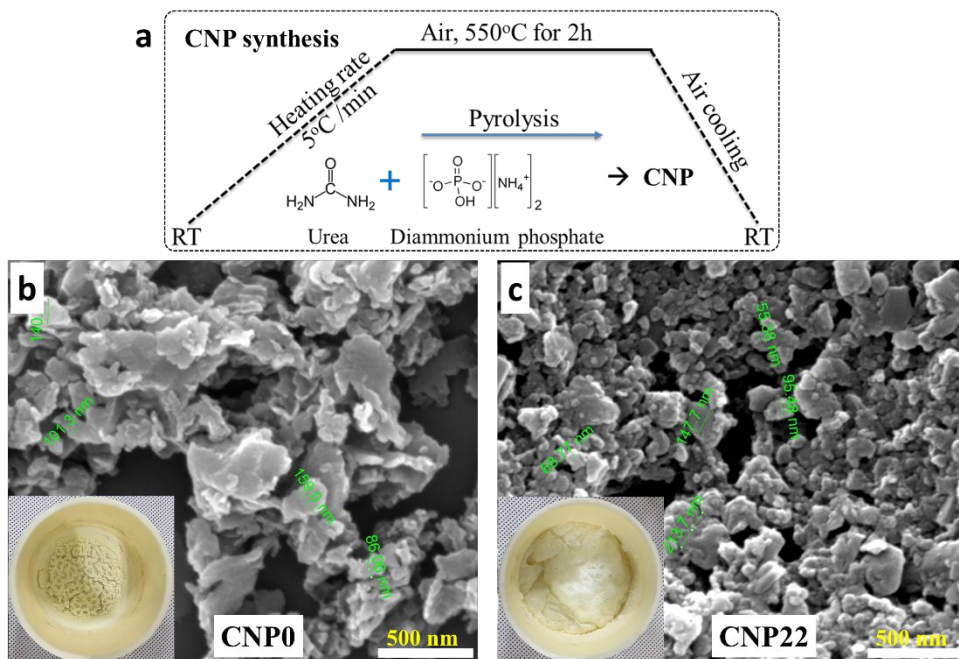
Supporting figures and tables

Figure S1. a) The synthesis process of CNP. b) and c) are SEM images of CNP0 and CNP22. The insets in b) and c) are the digital photographs of CNP0 and CNP22 as pyrolysis, respectively. CNP was synthesized *via* pyrolyzing $(NH_2)_2CO$ with $(NH_4)_2HPO_4$ at 550 °C for 2 hours.
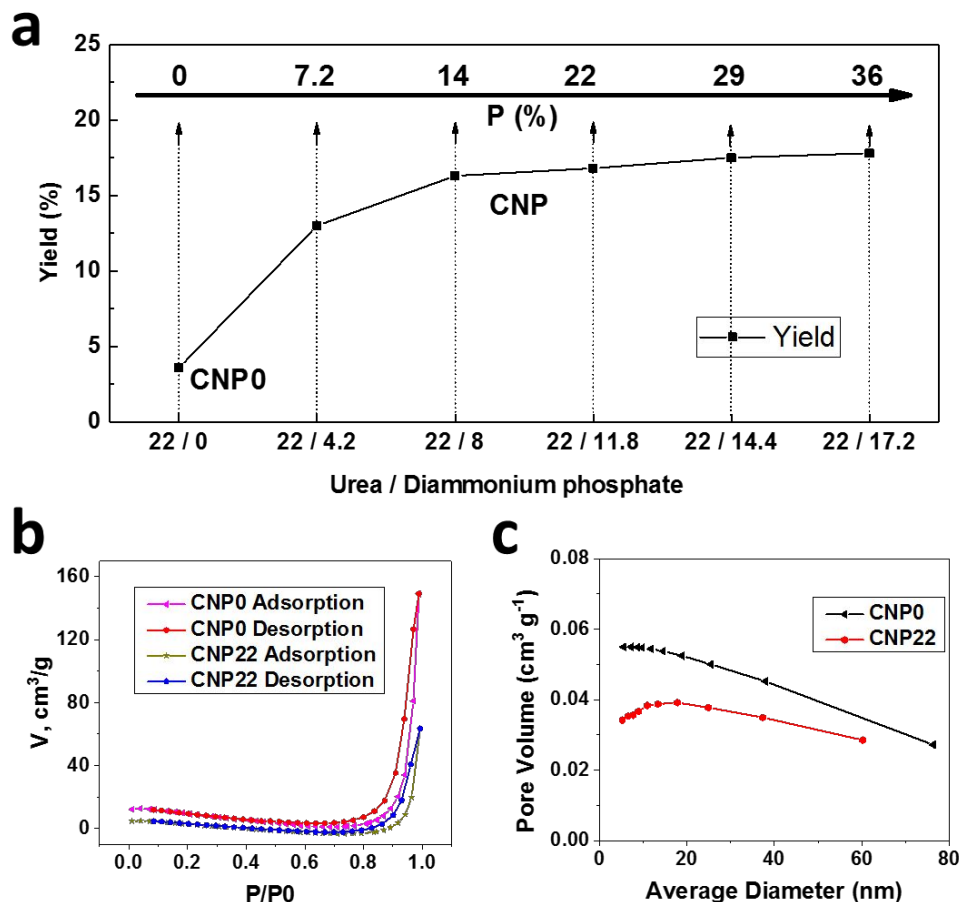
Figure S2. a) Yield of urea/diammonium phosphate pyrolysis corresponding to CNP0 and CNP with P concentrations from 7.2 to 36%. b) N_2 adsorption-desorption isotherms of CNP0 and CNP22 by the BET measurement. c) Pore-size distribution of CNP0 and CNP22 by the BJH measurement.

Herein, the yield of CNP0 after the urea pyrolysis at 550 °C for 2 hours is 3.6%, which is a higher yield than the ~1% in reported literatures that pyrolyzes urea in 3h.[7] Whereas CNP22 in the same synthesis process has 16.8% of yielding. Urea pyrolysis produces CNP0 with the highest surface area, without a template. However, this process also gives the lowest yield (~1%).[7] This method is therefore not suitable for large-scale production. Here, a combination of $(NH_2)_2CO$ and $(NH_4)_2HPO_4$ not only provides a porous structure but also increases the CNP yield by approximately 4.5 times (Figure S2a). N_2 adsorption-desorption isotherms (Figure S2b) show a slight decrease in the specific surface area of CNP (16 m^2 g^{-1}) compared to that of CNP0 (22 m^2 g^{-1}). Similarly, it is found that CNP has a smaller pore volume and pore size distribution than those

of CNP0 (Figure S2c). This finding may have occurred because of the decrease in the pore walls thickness in the presence of a new element (here, it is P) that leads to the collapse of the pore walls of carbon nitride, leading to a decrease in the surface area.[8] In addition, the significant decomposition of CNP0 at 550 °C (Figure S5) also decreases the particle size and increases the pore volume, resulting in an increase in surface area.[9]
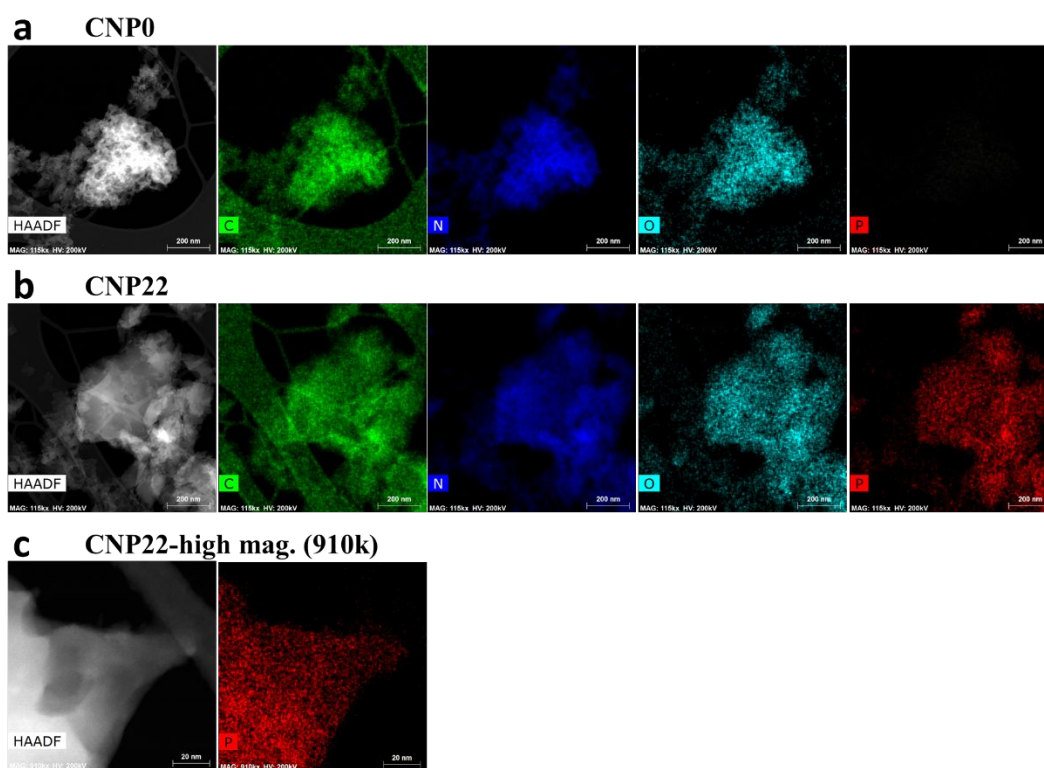

Figure S3. STEM mapping images were measured at 119k magnification for the a) CNP0 and b) CNP. From left to right, the images are the high-angle annular dark-field (HAADF), carbon, nitrogen, oxygen, and phosphorus elements. c) Mapping of phosphorus element in CNP at a high magnification (910K).
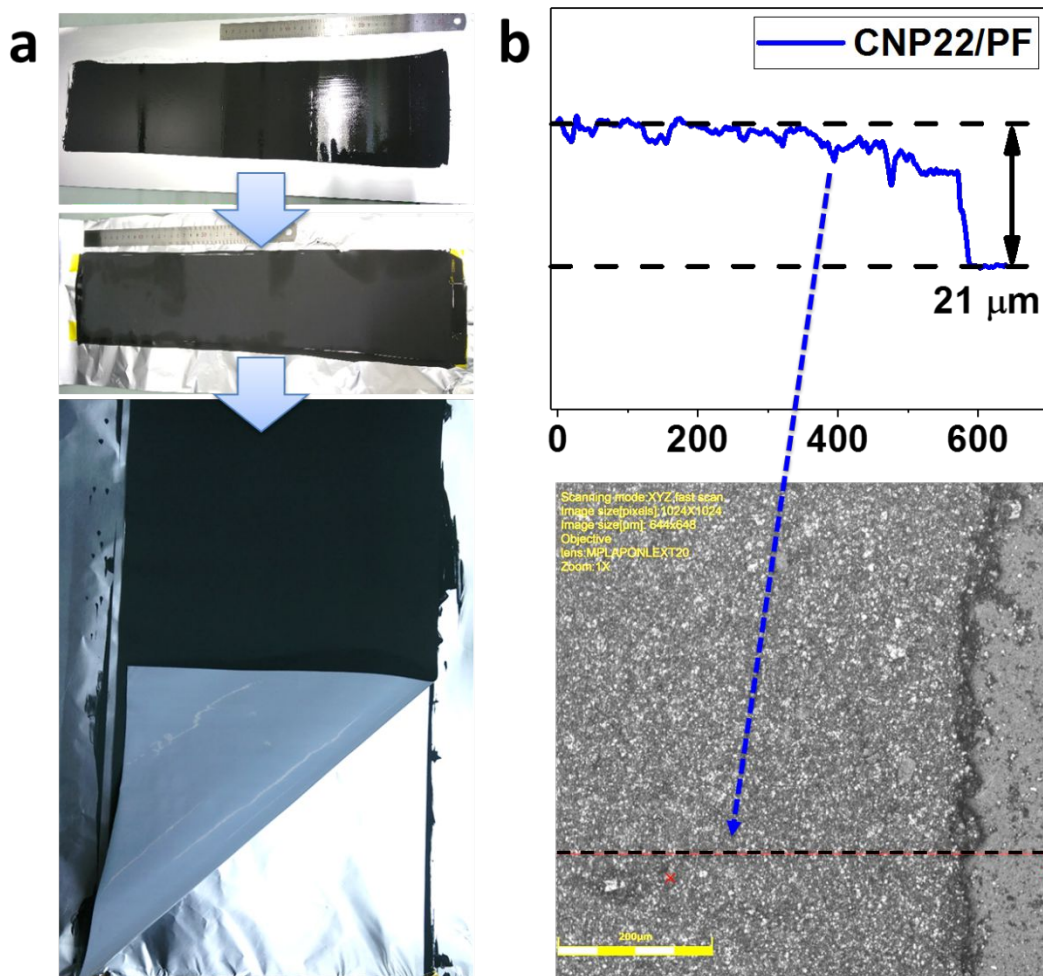
Figure S4. a) The CNP22/PF coating process, from top to bottom: as-casted, drying, and final CNP22/PF. b) The thickness of CNP22/C coated layer on PF and corresponding surface image measured by the step function on 3D laser microscope.
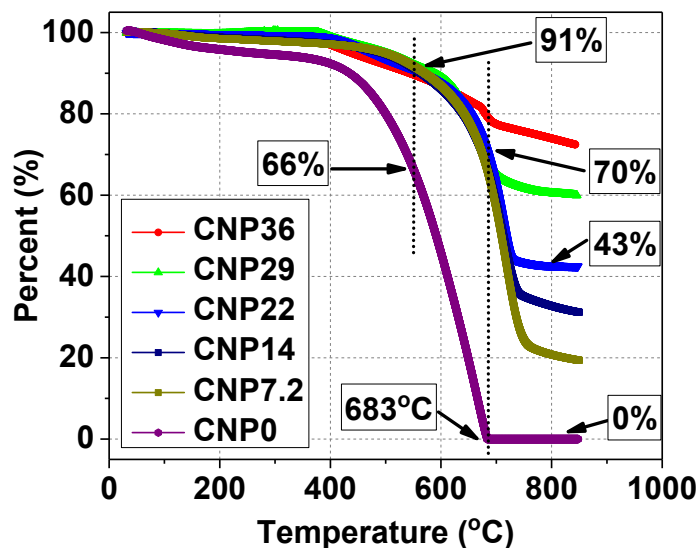
Figure S5. The thermal stability of the CNPx materials are evaluated by TGA with the temperature ranging from RT to 850 °C in N_2 ambient and a heating rate of 5 °C min^{-1}.
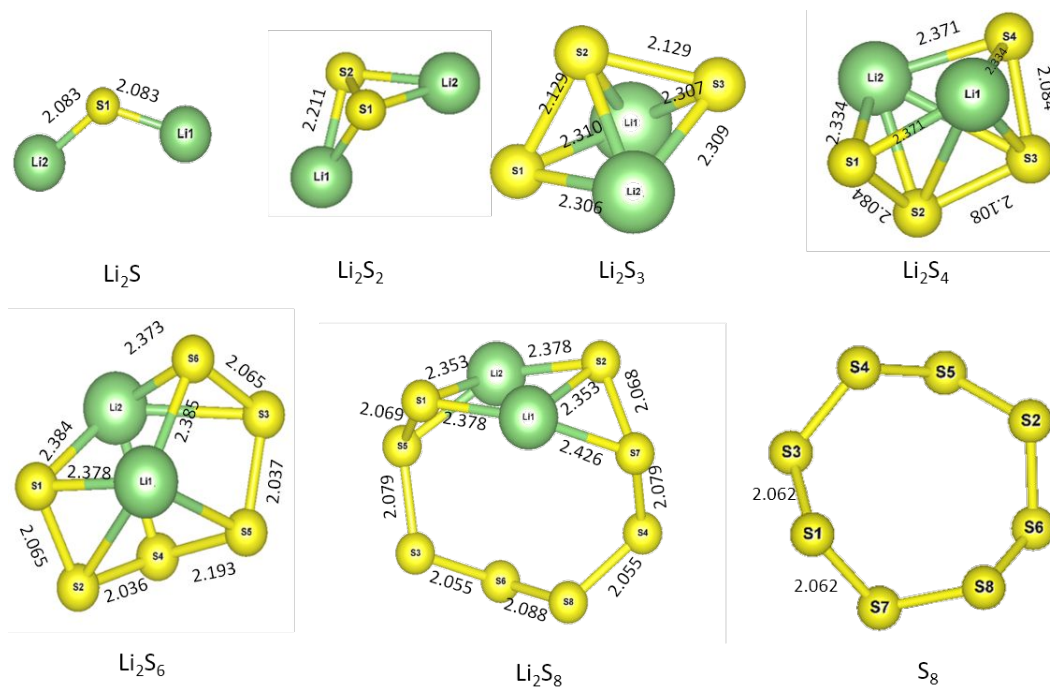

Figure S6. Molecular structures of various LiPS {Li_2S_x (x = 1, 2, 3, 4, 6, 8)} and S_8 molecule after the optimization along with the corresponding bond lengths. Yellow and green spheres represent S and Li atoms.
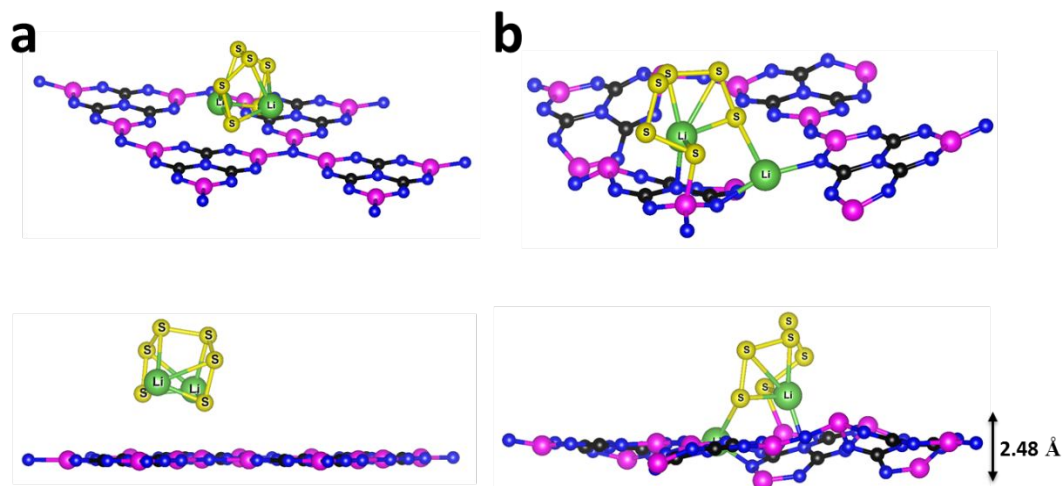
Figure S7. The adsorption of Li_2S_6 on CNP22 supercell. a) The top and cross-sectional view before the relaxation. b) The top and cross-sectional view after the relaxation. Buckling of the order of 2.48 Å was observed for the CNP22 sheet after the relaxation. Yellow, green, black, blue, and pink spheres represent S, Li, C, N, and P atoms, respectively.
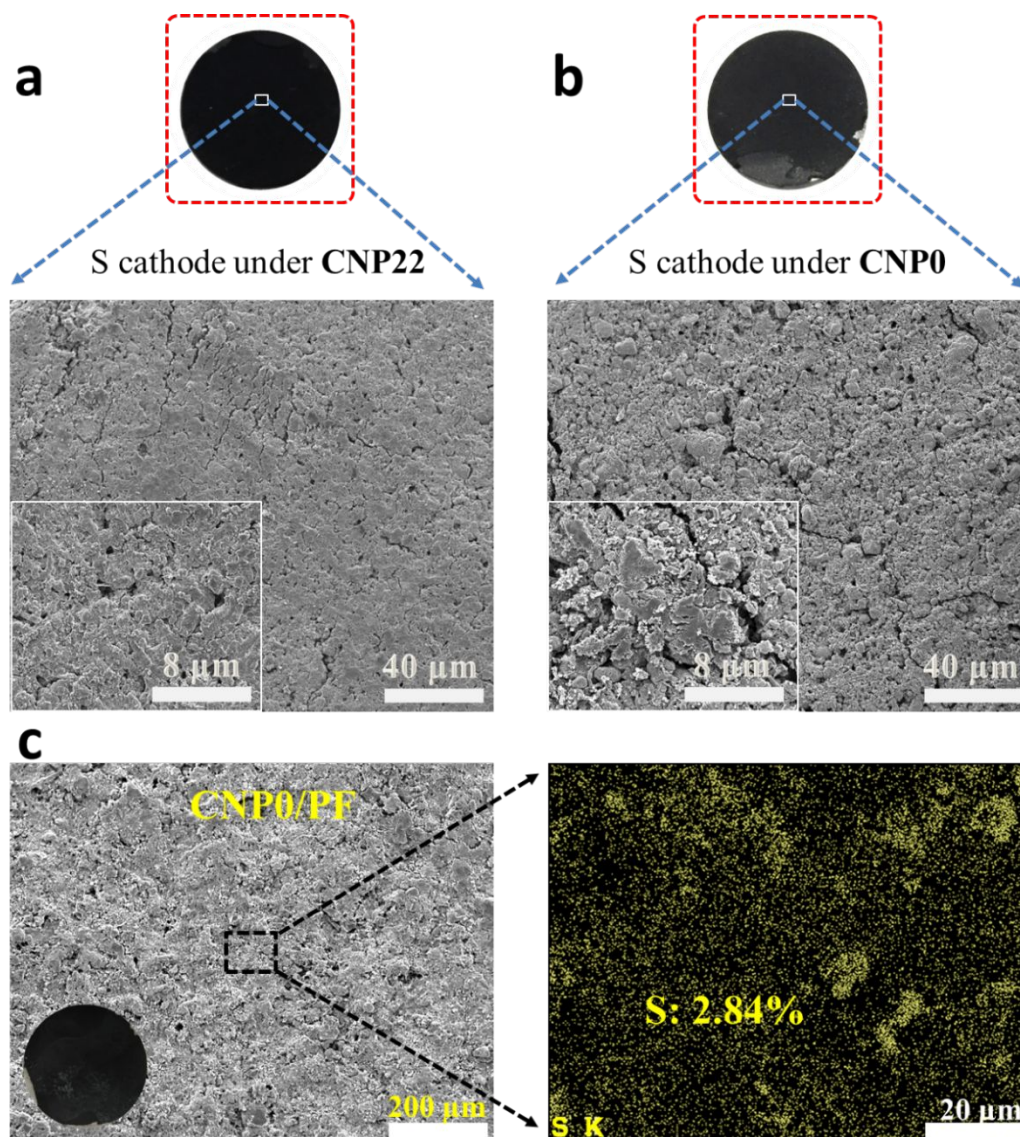
Figure S8. The digital photographs of the S cathode and corresponding SEM images of the cycled cathode with (a) CNP22/PF and (b) CNP0/PF. c) SEM image and S elemental mapping for CNP0/PF (right). The inset in part S8c shows a digital photograph of CNP0/PF after disassembling Li–S cell.

The Li–S cells were disassembled after the 100th cycle to analyze the S migrations from and on the S cathode, as well as the surface morphology of the S cathodes with CNP22/PF and CNP0/PF. After disassembling the cells, the S cathodes were soaked in, and washed several times with 1,3-dioxolane to remove impurities. When the samples were completely dry, SEM-EDX was used for surface examinations.
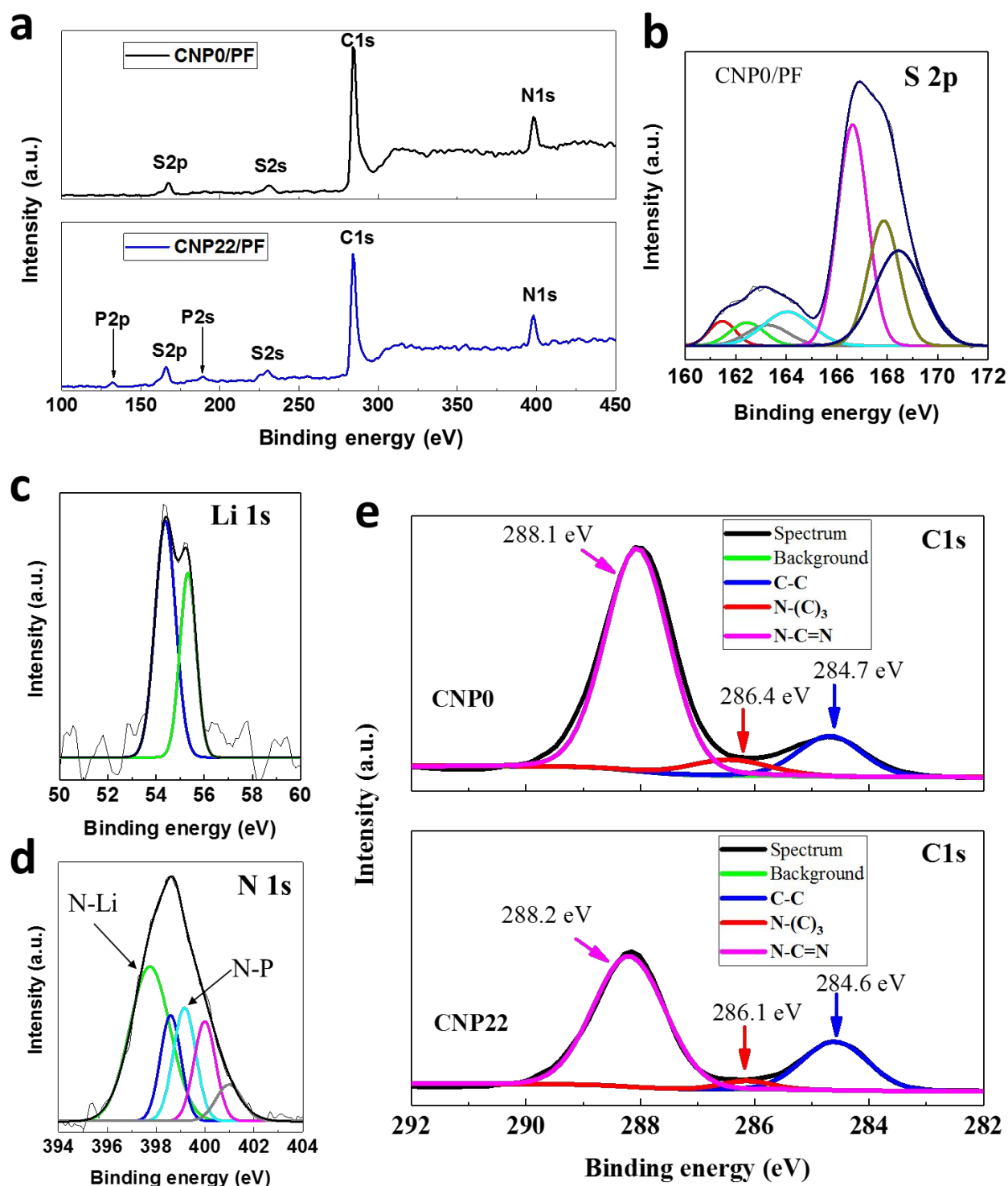
Figure S9. XPS spectra. a) The full-scan spectra show the presence of elements on the PF. b) S 2p scanning XP spectra for CNP0/PF. c) and d) The deconvolution of Li 1s and N 1s spectra of the Li|CNP22/PF|S cell after 100 cycles. e) The deconvolution of C 1s of CNP0 and CNP22 powder. The identified bonds in the C 1s spectra in our study matches the reported study.[10]

In addition to the bonds of P 2p and S 2p examined in the discussion section, we also investigated the binding components of Li 1s and N 1s to evaluate the overall effect of CNP22 on LiPS. The deconvolution of the Li 1s spectrum (Figure S9c) shows two peak positions at 54.7 and 55.5 eV that are Li–S and Li–N bonding peaks, respectively.[11] For the N 1s spectrum of the CNP22/PF sample (Figure S9d), the N–Li bond at the 397.7 eV peak position predominates in the five N components. Of the three peaks, the majors peaks are pyridinic N (398.6 eV) and pyrrolic N (400 eV), and a lower peak (401 eV) belongs to the graphitic N bonds. It is postulated that the peak close to the pyridinic N at 399.1 eV is the N–P bond.
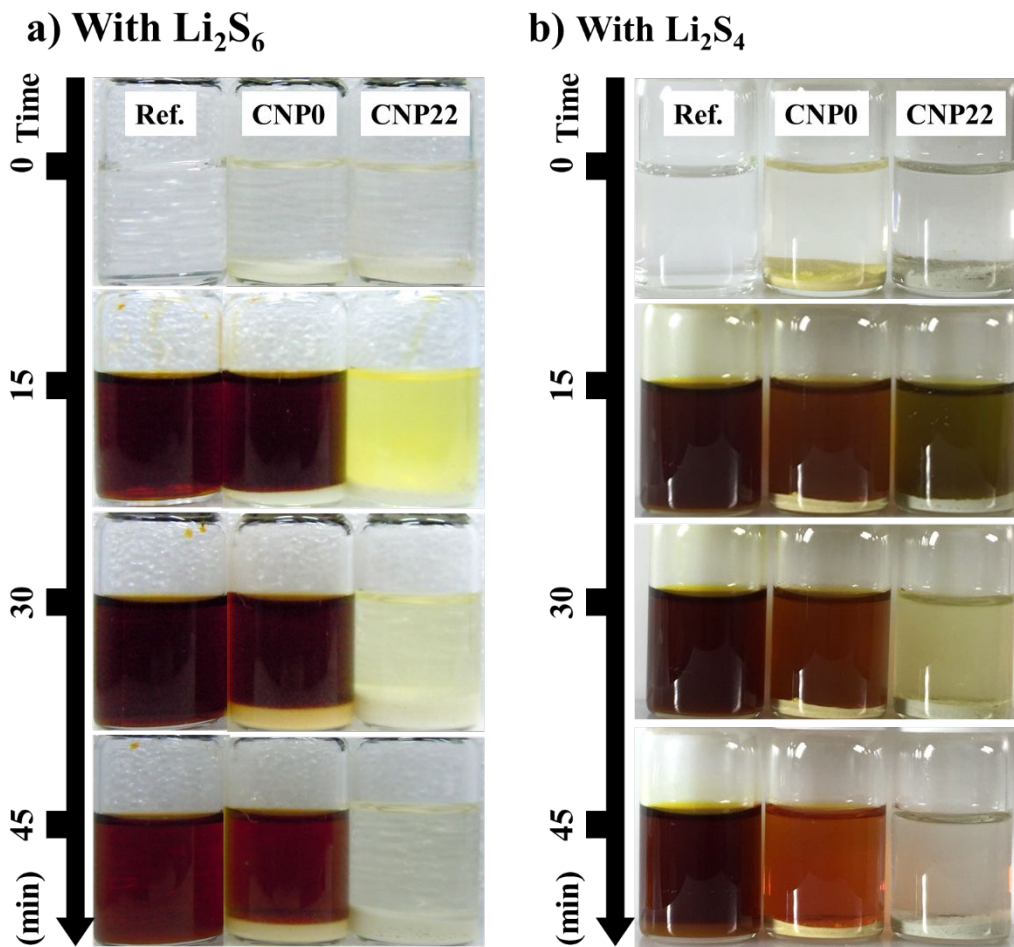

Figure S10. The LiPS adsorption experiment of a)Li_2S_6 and b) Li2S4 in the electrolyte with the presence of CNP0 and CNP22. In detail of part a), 50 mg of CNP0 and CNP22 were put into two vials, then 3 ml of

1M LiTFSI electrolyte was added to each vial. A vial containing the electrolyte only was used as a comparison object. 0.2 ml of 1M Li_2S_6 solution are added simultaneously to all 3 vials, and color change was recorded for every 15 min, 30 min and 45 min. Note that the solutions in Figure 2m were diluted ten times before UV-vis absorbance measurement to ensure the absorbance spectra of Li_2S_6 could be measured. Similarly, experiment was repeated in part b, except that LiPS were tested as Li_2S_4.
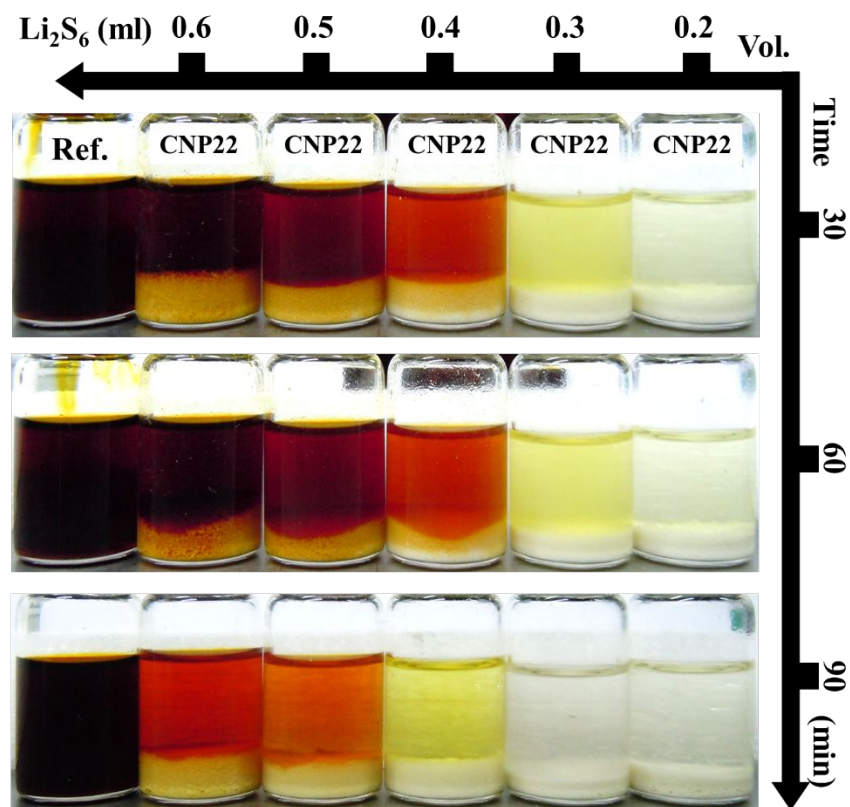
Figure S11. Observation on LiPS adsorbability of CNP22 based on the color change. Various amounts of 1M Li_2S_6 from 0.2 to 0.6 ml were added to the vials, which contain 50 mg CNP22 and 3 ml of 1M LiTFSI electrolyte each. A vial containing 3 ml electrolyte and 0.6 ml 1M Li_2S_6 was used as a comparison object. Color change was recorded for every 30 min, 60 min and 90 min.

Table S1. The variation of energy and the external pressure with increase in the lattice constant of unit cell of CNP22

Lattice constant (Å)	Energy (eV/unit cell)	External Pressure (kB)
7.10	-94.361	89.65
7.20	-96.301	75.17
7.40	-99.175	46.82
7.60	-100.902	24.60
7.70	-101.404	15.75
7.90	-101.920	5.82
8.10	-102.182	3.94
8.20	-102.285	3.63
8.40	-102.519	2.52
8.42	-102.533	1.94
8.44	-102.543	1.38
8.46	-102.550	0.82
8.48	-102.555	0.14
8.49	-102.556	0.00
8.495	-102.556	-0.14
8.50	-102.556	-0.26
8.52	-102.554	-0.79
8.54	-102.550	-1.30
8.58	-102.532	-2.28
8.60	-102.520	-2.75

Table S2. Bader charge analysis on the LiPS before and after adsorption on CNP22. Top row for each molecule represents the charge before adsorption (black), and the bottom row for after adsorption (red) on CNP22.

Molecule	Adsorption	Li1	Li2	S1	S2	S3	S4	S5	S6	S7	S8
Li_2S	Before	0.86	0.86	-1.72	-	-	-	-	-	-	-
	After	0.56	0.67	-0.54	-	-	-	-	-	-	-
Li_2S_2	Before	0.86	0.86	-0.86	-0.86	-	-	-	-	-	-
	After	0.54	0.59	0.09	-0.09	-	-	-	-	-	-
Li_2S_3	Before	0.86	0.86	-0.74	-0.23	-0.75	-	-	-	-	-
	After	0.59	0.48	-0.32	0.07	-0.47	-	-	-	-	-
Li_2S_4	Before	0.86	0.86	-0.69	-0.17	-0.70	-1.56	-	-	-	-
	After	0.46	0.53	-0.44	0.10	-0.25	0.07	-	-	-	-
Li_2S_5	Before	0.86	0.86	-0.65	-0.15	-0.15	-0.07	-0.67	-	-	-
	After	0.56	0.54	-0.56	0.42	0.02	-0.02	-0.07	-	-	-
Li_2S_6	Before	0.86	0.87	-0.69	-0.03	-0.05	-0.15	0.15	-0.67	-	-
	After	0.46	0.56	-0.20	-0.10	-0.06	0.08	0.04	-0.37	-	-
Li_2S_7	Before	0.86	0.86	-0.65	-0.03	-0.04	-0.01	-0.14	-0.15	-0.68	-
	After	0.53	0.39	-0.13	-0.01	-0.02	-0.00	0.01	0.03	-0.34	-
Li_2S_8	Before	0.86	0.86	-0.66	-066	0.00	0.00	-0.16	-0.03	-0.15	-0.03
	After	0.48	0.58	-0.42	-0.57	0.07	-0.05	-0.12	-0.10	0.11	0.10

Table S3. Volumetric energy density (VED) of Li|CNP22/PF|S cell (at the 288th cycle, capacity: 4.742 mAh) and Li|PF|S cell (at the 159th cycle, capacity: 2.773 mAh)

Volumetric energy density (Wh L^{-1})				
Components of the Li|CNP22/PF|S cell (#1)	CNP22/PF	S cathode	Li anode	Electrolyte
Thickness (μm)	(25 + 21)	78	100	x
Volume (cm^3)	(46*0.92 + 78*0.72 + 100*0.752)*π*10^{-4} = 0.0413			
VED$_{\#1}$	(4.742*2.2) / 0.036 = **252**			
Components of the Li|PF|S cell (#2)	Pristine PF	S cathode	Li anode	Electrolyte
Thickness (μm)	25	78	100	x
Volume (cm^3)	(25*0.92 + 78*0.72 + 100*0.752)*π*10^{-4} = 0.036			
VED$_{\#2}$	(2.773*2.2) / 0.036 = **169**			

Table S4. Gravimetric energy density (GED) of Li|CNP22/PF|S cell (at the 288th cycle, capacity: 4.742 mAh) and Li|PF|S cell (at the 159th cycle, capacity: 2.773 mAh)

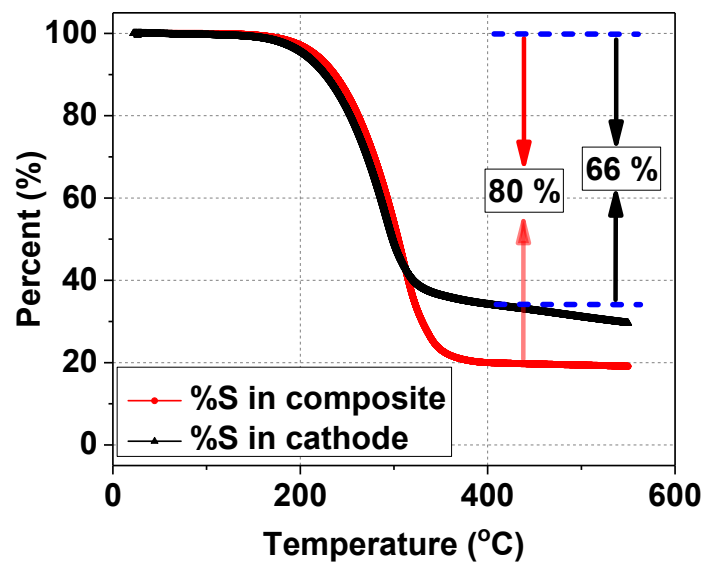| Gravimetric energy density (Wh kg^{-1})				
Components of the Li|CNP22/PF|S cell (#1)	CNP22/PF	S cathode	Li anode	Electrolyte
Weight (mg)	(2.7 + 1.4)	7.46	9.4	30
Total weight (g)	(2.7 + 1.4 + 7.46 + 9.4 + 30)*10^{-3} = 0.05096			
GED$_{\#1}$	(4.742*2.2) / 0.05096 = **205**			
Components of the Li|PF|S cell (#2)	Pristine PF	S cathode	Li anode	Electrolyte
Weight (mg)	2.7	7.46	9.4	25
Total weight (g)	(2.7 + 7.46 + 9.4 + 25)*10^{-3} = 0.04456			
GED$_{\#2}$	(2.773*2.2) / 0.04456 = **137**			

Figure S12. The percentage of pure S in the S/C composite and in the cathode measured via TGA from RT to 550 °C in N_2 ambient with the heating rate of 5 °C min^{-1}.
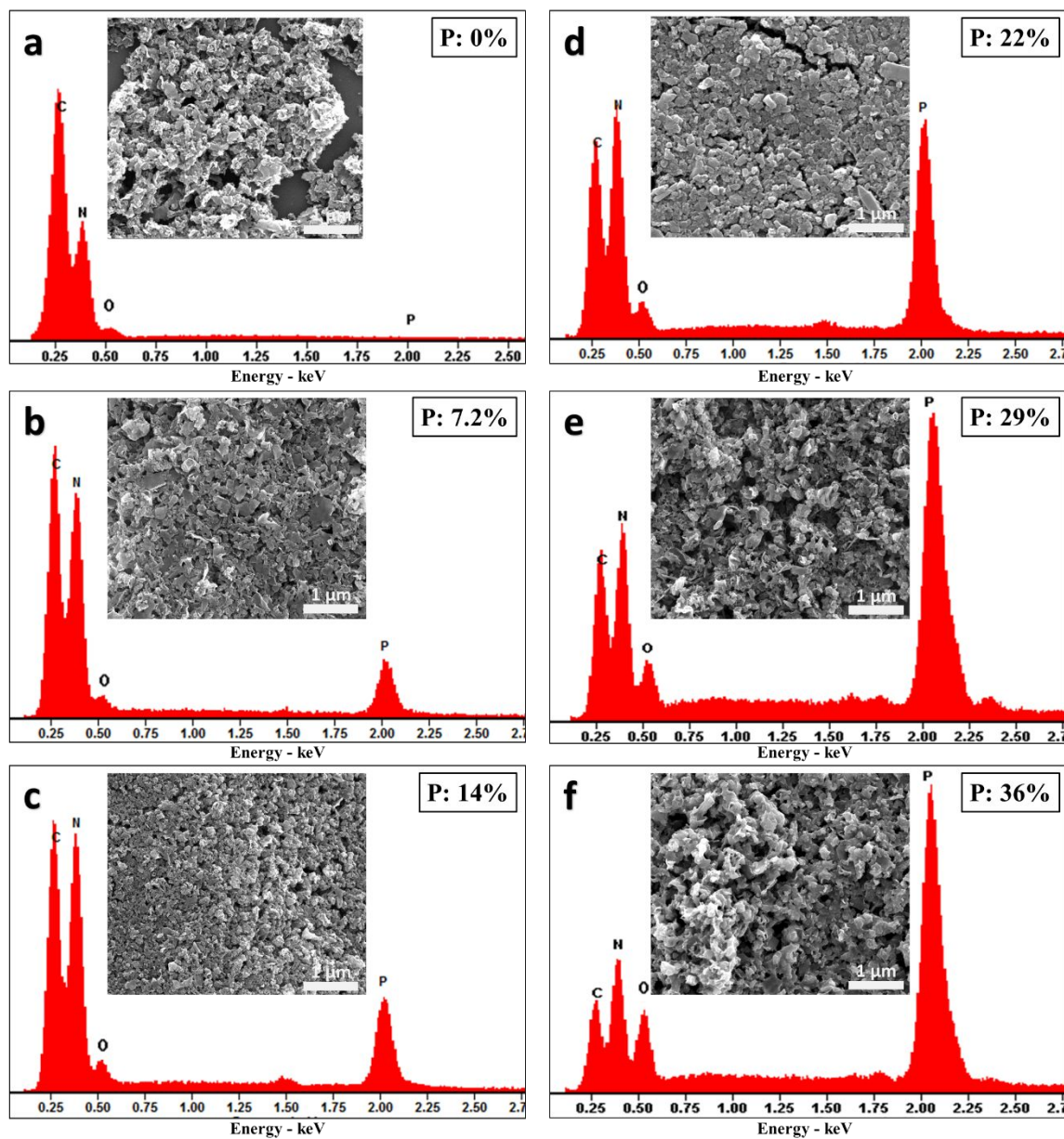
Figure S13. SEM and corresponding EDX measurements of various concentrations of P in CNP. a) CNP0, b) CNP7.2, c) CNP14, d) CNP22, e) CNP29, and f) CNP36.
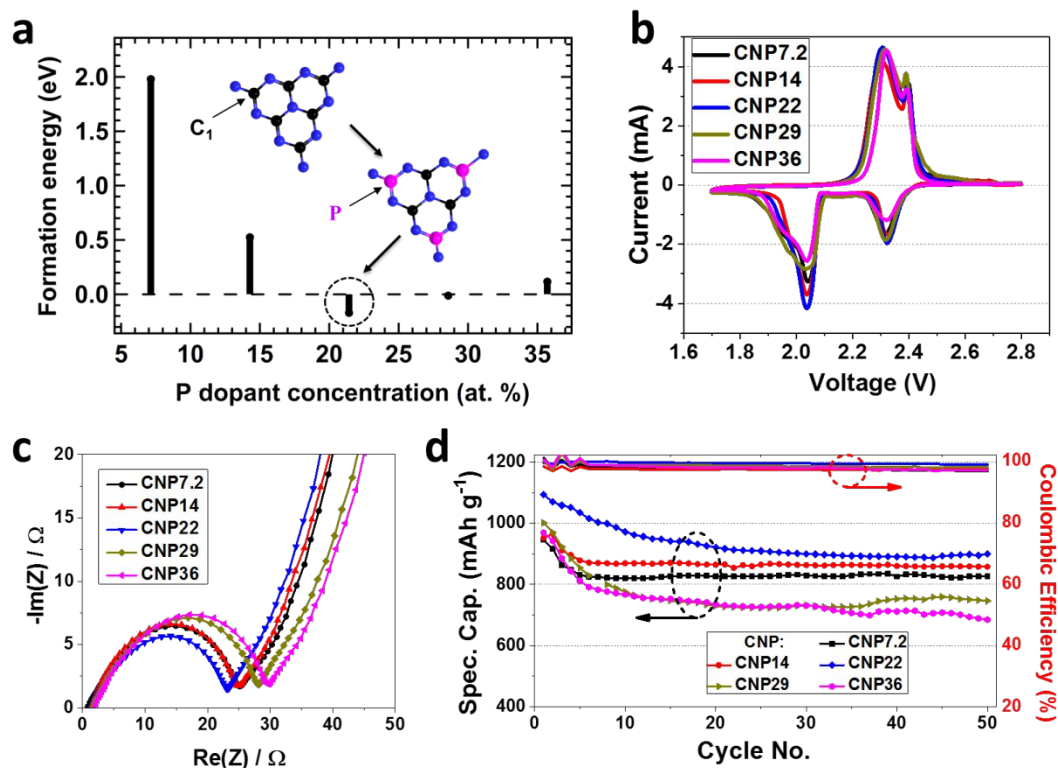
Figure S14. Optimization of P concentration in CNP. a) Plot of formation energy per P atom with respect to varying P concentration. Black circle at 22% P shows favorable substitution percentage, corresponding to exothermic process. b), c), and d) are CV, EIS, and cycling performance, respectively, for Li–S batteries with CNPx/PF, with increasing P concentration from 7.2% to 36%. All Li–S cells had cathode with S loading of 3.2 mg cm^{-2}.

Reference

(1) Perdew, J. P.; Wang, Y. Pair-Distribution Function and Its Coupling-Constant Average for The Spin-Polarized Electron Gas. *J Physical Review B* **1992,** *46*, 12947.

(2) Kumar, T. D.; Shukla, A.; Kumar, R. Edge Configurational Effect on Band Gaps in Graphene Nanoribbons. *Physical Review B* **2015,** *91*, 115428.

(3) Kumar, S.; Shukla, A.; Kumar, R. Origin of Multiple Band Gap Values in Single Width Nanoribbons. *Scientific reports* **2016,** *6*, 36168.

(4) Monkhorst, H. J.; Pack, J. D. Special Points for Brillouin-Zone Integrations. *Physical Review B* **1976,** *13*, 5188-5192.

(5) Zhang, Q.; Wang, Y.; Seh, Z. W.; Fu, Z.; Zhang, R.; Cui, Y. Understanding The Anchoring Effect of Two-Dimensional Layered Materials for Lithium–Sulfur Batteries. *Nano letters* **2015,** *15*, 3780-3786.

(6) Huang, J.-Q.; Zhang, Q.; Peng, H.-J.; Liu, X.-Y.; Qian, W.-Z.; Wei, F. Ionic Shield for Polysulfides Towards Highly-Stable Lithium–Sulfur Batteries. *Energy Environ. Sci.* **2014,** *7*, 347-353.

(7) Zhang, W.; Zhang, Q.; Dong, F.; Zhao, Z. The Multiple Effects of Precursors on The Properties of Polymeric Carbon Nitride. *Int. J. Photoenergy* **2013,** *2013*.

(8) Cui, Y.; Zhang, J.; Zhang, G.; Huang, J.; Liu, P.; Antonietti, M.; Wang, X. Synthesis of Bulk And Nanoporous Carbon Nitride Polymers from Ammonium Thiocyanate for Photocatalytic Hydrogen Evolution. *J. Mater. Chem* **2011,** *21*, 13032-13039.

(9) Zhang, G.; Zhang, J.; Zhang, M.; Wang, X. Polycondensation of Thiourea Into Carbon Nitride Semiconductors as Visible Light Photocatalysts. *J. Mater. Chem* **2012,** *22*, 8083-8091.

(10) Rajkumar, C.; Veerakumar, P.; Chen, S.-M.; Thirumalraj, B.; Lin, K.-C. Ultrathin Sulfur-Doped Graphitic Carbon Nitride Nanosheets As Metal-Free Catalyst for Electrochemical Sensing and Catalytic Removal of 4-Nitrophenol. *ACS Sustainable Chem. Eng.* **2018,** *6*, 16021-16031.

(11) Seh, Z. W.; Wang, H.; Hsu, P.-C.; Zhang, Q.; Li, W.; Zheng, G.; Yao, H.; Cui, Y. Facile Synthesis of Li2s–Polypyrrole Composite Structures for High-Performance Li2s Cathodes. *Energy Environ. Sci.* **2014,** *7*, 672-676.